Nanoscale Advances

ROYAL SOCIETY OF CHEMISTRY

PAPER

View Article Online
View Journal | View Issue

Cite this: *Nanoscale Adv.*, 2025, **7**, 6017

A novel nanocomposite Lf-DA-MSN-PF127 aided the delivery of dopamine for the treatment of Parkinson's disease in a rat model

Ramesha Hanumanthappa,[a] Sumit Ramesh Naik,[a] Sahana Prakash Nayak,[a] Asmatanzeem Bepari,[b] Hanan Nasser Altamimi,[c] Mujeeb Ahmed Shaikh,[d] Fahd A. Nasr,[e] Farha M. Shaikh,[d] P. C. Nethravathi,[fg] Hemalatha Nanjaiah,*[ah] D. Suresh,[fg] Raghu S. V.[i] and Kuramkote Shivanna Devaraju*[a]

Dopamine is a pivotal neurotransmitter in the central nervous system, which is instrumental in motor functions. Parkinson's Disease (PD) is a chronic, progressive, age-related neurodegenerative disorder marked by the progressive loss of dopaminergic neurons in the pars compacta of the *substantia nigra* in the midbrain, resulting in the reduction of dopamine levels. Levodopa is a prescribed medicine for symptomatic relief of PD, as it is an amino acid precursor of dopamine that readily crosses the Blood–Brain Barrier (BBB). However, levodopa exhibits poor plasma bioavailability and limited brain uptake, and induces peripheral side effects. To overcome this biological impediment, we have developed and characterized a lactoferrin-functionalized Pluronic F-127 capped dopamine-loaded mesoporous silica nanocomposite (Lf-DA-MSN-PF127) to furnish dopamine across the BBB. *In vivo* experiments using a rotenone (ROT) induced PD rat model confirmed that Lf-DA-MSN-PF127 crosses the BBB and delivers dopamine. It remarkably boosts motor symptoms and dopamine levels in ROT-induced PD rats. Our study illustrates the nontoxic effect of the Lf-DA-MSN-PF127 nanocomposite and its efficacy in delivering dopamine across the BBB, providing a novel treatment strategy for PD.

Received 16th June 2025
Accepted 28th July 2025

DOI: 10.1039/d5na00593k

rsc.li/nanoscale-advances

1 Introduction

Parkinson's disease (PD) is one of the common and multifactorial neurodegenerative disorders (ND).[1] A key neuropathological feature of PD is progressive degeneration of dopamine neurons in the pars compacta of the *substantia nigra* in the midbrain, resulting in the reduction of the dopamine (DA) level.[2] In this condition, patients have defective motor behaviour,[3] such as rigidity, bradykinesia, resting tremor, and gait impairment.[4] Additionally, there are deficiencies in several non-dopaminergic neurotransmitter systems, including the cholinergic, serotonin, and noradrenergic systems, affecting various neuronal networks and brain regions, leading to non-motor symptoms.[5] So far, there has been no effective treatment that could halt the dopaminergic neurons' degeneration or restore their function. However, dopamine precursor and dopamine agonist drugs such as levodopa,[6,7] ropinirole,[8] pramipexole,[9] rotigotine,[10] entacapone,[11] opicapone,[12] rasagiline,[13] trihexyphenidyl, benztropine,[14] *etc.*, are prescribed to reduce the symptoms of PD. However, these medications have shown various side effects, including poor pharmacokinetic properties, anomalous spontaneous movements, rapid eye movement, sleep disturbances, dyskinesia, psychiatric complications, and wearing-off effect, and with prolonged use in advanced stages of the disease, these drugs lose their effectiveness.[15] Thus, it causes therapeutic failure in the effective treatment of PD.

Dopamine (DA), the neurotransmitter, is crucial for effectively managing PD symptoms. However, direct administration of DA is not possible due to its hydrophilic nature that prevents it from crossing the blood–brain barrier (BBB).[16] Effective treatment of PD requires the continuous and safe delivery of dopamine across the BBB. Therefore, developing new

[a]*Neurochemistry Lab, Department of Biochemistry, Karnatak University, Dharwad, Karnataka-580003, India. E-mail: ksdevaraju@kud.ac.in*

[b]*Department of Basic Health Sciences, College of Medicine, Princess Nourah bint Abdulrahman University, Riyadh 11671, Saudi Arabia*

[c]*Department of Medical Laboratory, College of Applied Medical Sciences, Prince Sattam bin Abdulaziz University, Al-Kharj 11942, Saudi Arabia*

[d]*Department of Basic Medical Science, College of Medicine, Al-Maarefa University, Diriyah, 13713, Riyadh, Saudi Arabia*

[e]*Department of Biology, College of Science, Imam Mohammad Ibn Saud Islamic University (IMSIU), Riyadh 11623, Saudi Arabia*

[f]*Department of Chemistry, University College of Science, Tumkur University, Tumkur, Karnataka 572103, India*

[g]*Department of Studies and Research in Organic Chemistry, Tumkur University, Karnataka 572118, India*

[h]*Department of Microbiology and Immunology, University of Maryland School of Medicine, 685W. Baltimore St. HSFI-380, Baltimore, Maryland 21201, USA. E-mail: hnanjaiah@som.umaryland.edu*

[i]*Division of Neuroscience, Yenepoya Research Centre (YRC), Yenepoya (Deemed to be University), Mangalore, Karnataka-575018, India*

pharmaceutical formulations that enable the transport and delivery of DA across the BBB is a priority. In this context, the drug-delivery (DD) strategy is gaining attention for its latent ability to penetrate the BBB and reach the target in the brain.[17]

Mesoporous silica nanoparticles (MSNs) are widely used as nanocarriers due to their biocompatibility, high drug loading capacity, large surface area, adjustable pore size, and ease of surface modification. They have been successfully employed to deliver drugs like doxorubicin, nerve growth factor, temozolomide, and phytochemicals for treating neurological disorders. However, a key limitation of MSNs is premature drug release. To address this, surface capping with polymers such as Pluronic F127 (PF127) is used to control and target drug release. PF127 is an FDA-approved, non-toxic, biodegradable, thermosensitive triblock copolymer comprising hydrophilic poly(ethylene oxide) (PEO) and hydrophobic poly(propylene oxide) (PPO)[18,19] and is commonly used in drug delivery, cancer therapy, vaccines, and intranasal formulations.[20,21] Lactoferrin (Lf) is an iron-binding, multifunctional cationic glycoprotein.[22] It is found in various human secretions[23] and interacts with lactoferrin receptors (LfR) on respiratory epithelial and brain endothelial cells.[22,24] Notably, LfR is overexpressed in neurodegenerative disorders such as Alzheimer's disease, PD, Huntington's disease, and amyotrophic lateral sclerosis,[25] facilitating enhanced brain uptake of Lf. Leveraging this, we modified PF127-coated MSN nanoparticles with Lf to enable receptor-mediated dopamine delivery to the brain.

In the present study, we have developed a lactoferrin-functionalized PF127-capped dopamine-loaded mesoporous silica nanocomposite (Lf-DA-MSN-PF127). The synthesized nanocomposite was characterized using techniques such as XRD, UV-DRS, zeta size, zeta potential, Fourier-transform infrared spectroscopy (FTIR), Brunauer–Emmett–Teller (BET), field-emission scanning electron microscopy (FE-SEM), energy-dispersive X-ray spectroscopy (EDS), and high-resolution transmission electron microscopy (HR-TEM) with selected area electron diffraction (SAED). Furthermore, we determined the *in vitro* toxicity of the synthesized nanocomposite and studied its delivery into the brain in a rat model. Its effect of restoring neurobehavioral and neurotransmitter release in the rotenone (ROT)-induced PD rat model was tested.

2 Results and discussion

2.1. Synthesis and characterization

We prepared Lf-DA-MSN-PF127 NC for the successful delivery of DA across the BBB using intranasal administration. In the current study, after DA loading into the MSN to prevent the premature release of dopamine from MSN, we capped PF127 on the surface of DA-MSN. Additionally, we functionalized the surface of DA-MSN-PF127 with Lf to facilitate the successful penetration of the BBB (Scheme 1). The average size and polydispersity index (PDI) of the synthesised NC were determined using the dynamic light scattering technique (DLS), and the resulting data are shown in Fig. 1A–C. The data revealed that the average size of the MSNs, DA-MSN-PF127, and Lf-DA-MSN-PF127 was found to have a *Z* average of 114.4 nm (Fig. 1A), 229.9 nm (Fig. 1B), and 268.3 nm (Fig. 1C) with a PDI of 0.325, 0.229, and 0.354, respectively. This suggested narrow particle size distribution of the developed nanocomposites (NCs) and a homogenous population. The average size of DA-MSN-PF127 and Lf-DA-MSN-PF127 was found to be slightly increased

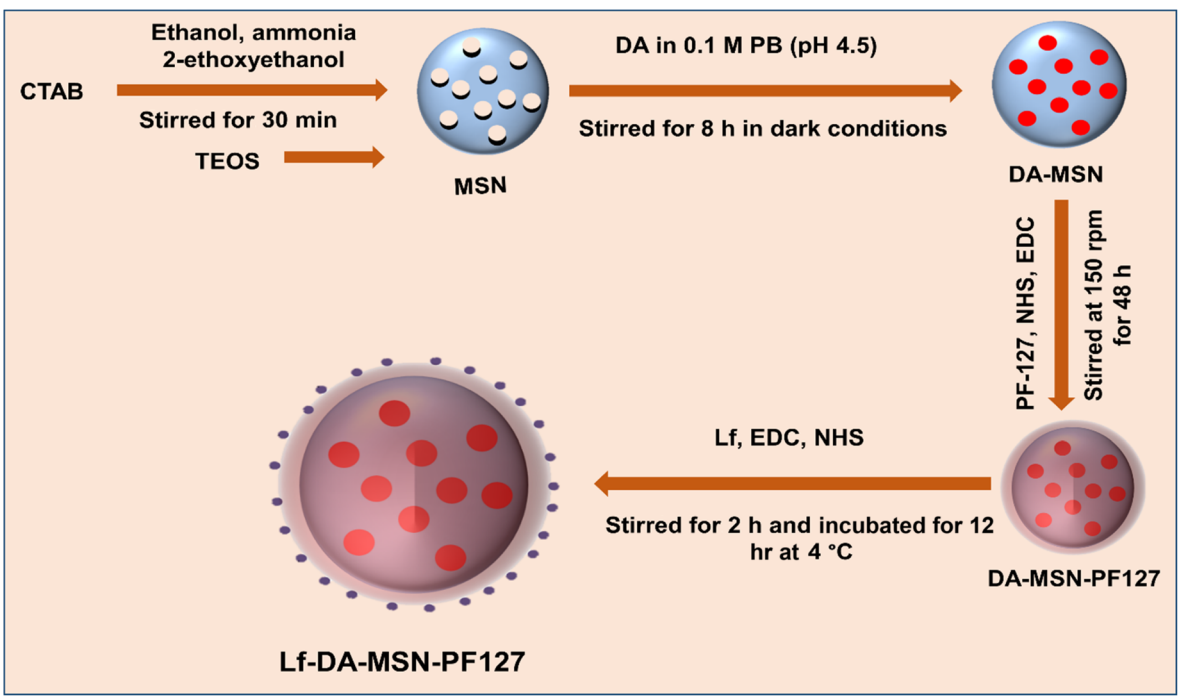

Scheme 1 Schematic representation of the synthesis of MSN, DA-MSN, DA-MSN-PF127 and Lf-DA-MSN-PF127.

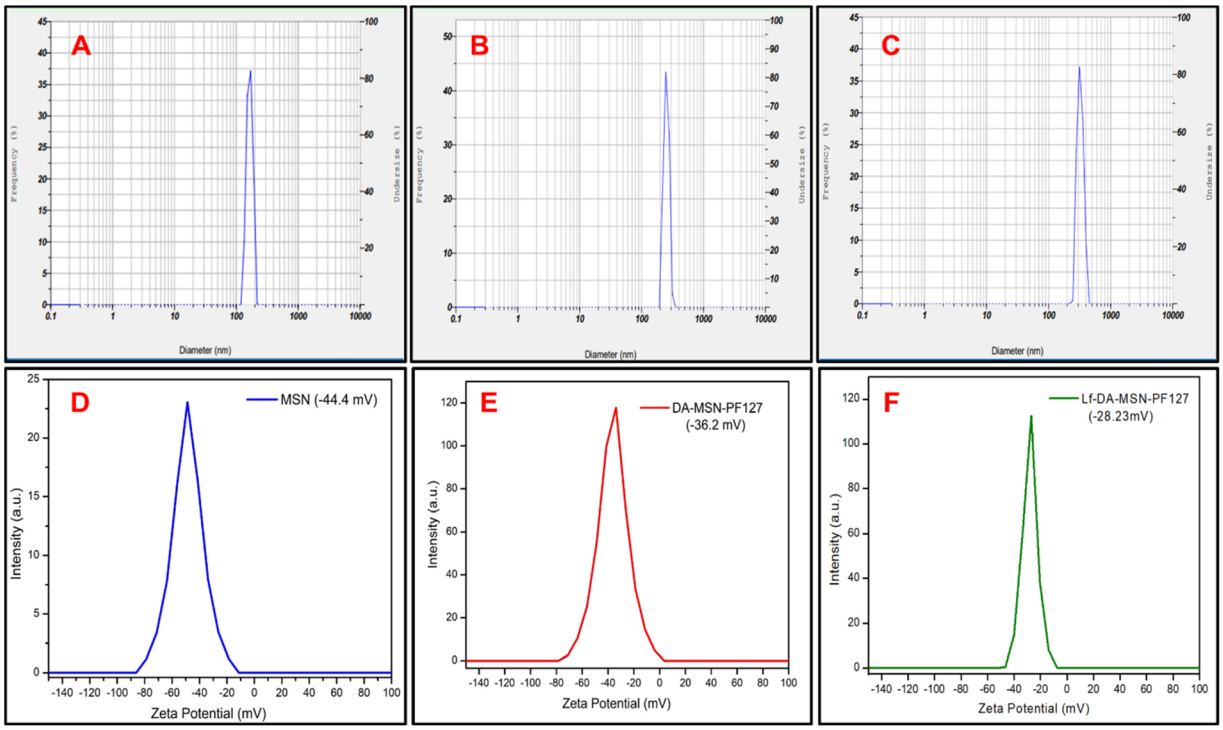

Fig. 1 Zeta *Z* average size of (A) MSN NPs, (B) DA-MSN-PF127 NC, (C) Lf-DA-MSN-PF127 NC and zeta potential of (D) MSN NPs, (E) DA-MSN-PF127 NC and (F) Lf-DA-MSN-PF127 NC.

compared to the MSNs, which is due to the conjugation of Lf and PF127 with MSNs. The physical stability of the colloidal dispersion of the synthesised NCs was analysed through zeta potential as shown in Fig. 1D–F. The zeta potential values of MSNs, DA-MSN-PF127, and Lf-DA-MSN-PF127 were found to be −44.4 mV (Fig. 1D), −36.2 mV (Fig. 1E), and −28.23 mV (Fig. 1F). The layers of polymer and protein formed on the surface of the nanoparticles[30] influenced the electrostatic interactions with the surrounding medium and modified the existing interactions on the metal oxide nanoparticle surface.[31] As a result of this, the zeta potential of the MSNs decreased after binding to lactoferrin (Lf) and Pluronic F127 (PF127). However, the data indicate that the synthesised NCs have sufficient repulsive force to attain better physical colloidal stability in an aqueous solution.

Fig. 2A illustrates the UV-DRS plot of MSNs, DA, PF127, and Lf. To acquire the Kubelka–Munk UV-DRS graph, the change in altered energy was plotted against the Kubelka–Munk function. The band gap of MSNs, DA, PF127, and Lf has been estimated to be 3.8, 2.1, 2.2, and 2.5 eV, respectively (Fig. 2B).[26–29]

Fig. 2C and D show the MSN pore size range and nitrogen gas adsorption–desorption isotherms. The Barrett–Joyner–Halenda (BJH) technique was used to calculate the range of pore sizes derived from the isotherms. Fig. 2C simulates the H1 B–H loop from P/P_0, which is linked to the presence of uniform mesopores. Based on the curve's shape, it was noticed that the resultant MSNs displayed type IV adsorption–desorption isotherms. Furthermore, the Brunauer–Emmett–Teller (BET) equation was employed to estimate the specific surface area and pore volume of the MSNs, which were found to be 235.3 $m^2\ g^{-1}$ and 0.62 $cm^3\ g^{-1}$, respectively. From Fig. 2D, the pore diameter of MSN s was calculated, which was found to be 2.83 nm.

Fig. 3 illustrates the XRD patterns of MSN, DA-MSN-PF127, and Lf-DA-MSN-PF127. The amorphous nature of MSNs is responsible for a broad peak appearing at 22.5°.[32] The XRD pattern of DA-MSN-PF-127 exhibited the characteristic peak of dopamine with 2θ values of 23.8, 28.32, 29.5, 30.70, 33.79, 38.31, 40.69, and 46.69, which were well matched with the JCPDS # 08-0247 card.[33] This ensures the successful loading of dopamine to MSNs. Furthermore, from the XRD pattern of Lf-DA-MSN-PF127, it was clear that the peaks due to dopamine were not disturbed upon binding of Lf to DA-MSN-PF127.

Fig. 4 depicts the FTIR spectrum of the synthesised MSNs, DA, PF127, Lf, DA-MSN, DA-MSN-PF127, and Lf-DA-MSN-PF127. Peaks positioned at 1044, 803 and 439 cm^{-1} were identified in the FTIR spectrum of MSN as corresponding to the asymmetrical Si–O–Si stretching, symmetrical Si–O–Si stretching and O–Si–O bending patterns in MSNs, respectively. Whereas, the band at 950 cm^{-1} was attributed to Si–OH groups and the peak at 1642 cm^{-1} was attributed to the moisture adsorbed on the silicon dioxide component.[34] The FTIR spectrum of dopamine showed bands at 1615 and 3425–3480 cm^{-1} due to adsorbed water and hydroxyl molecules at the interface.[35] The bands appearing at 2942 and 2824 cm^{-1} were ascribed to the stretching of aromatic C–H, whereas the bands at 1487 and 1497 cm^{-1} were ascribed to the bending of aromatic C–H. Similarly, the bands at 1271, 1124, and 1612 cm^{-1} were assigned to C–O stretching, C–H bending of the aliphatic group, and N–H

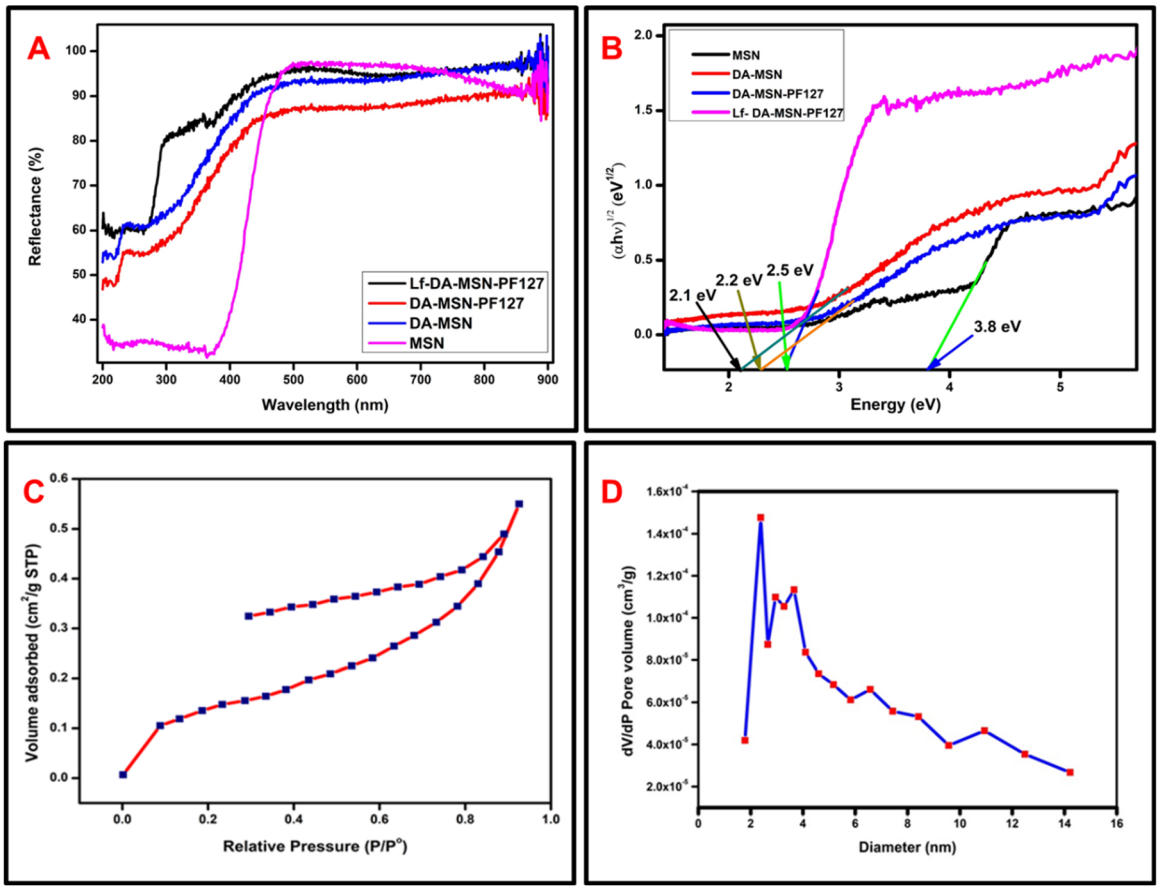

Fig. 2 (A) UV-Visible diffuse reflectance spectra of MSNs, DA-MSN, DA-MSN-PF127 NC, and Lf-DA-MSN-PF127 NC and (B) Kubelka–Munk plot of MSNs, DA-MSN, DA-MSN-PF127 NC, and Lf-DA-MSN-PF127 NC. (C) Nitrogen gas adsorption–desorption isotherms for MSNs and (D) pore size distribution obtained from adsorption measurements.

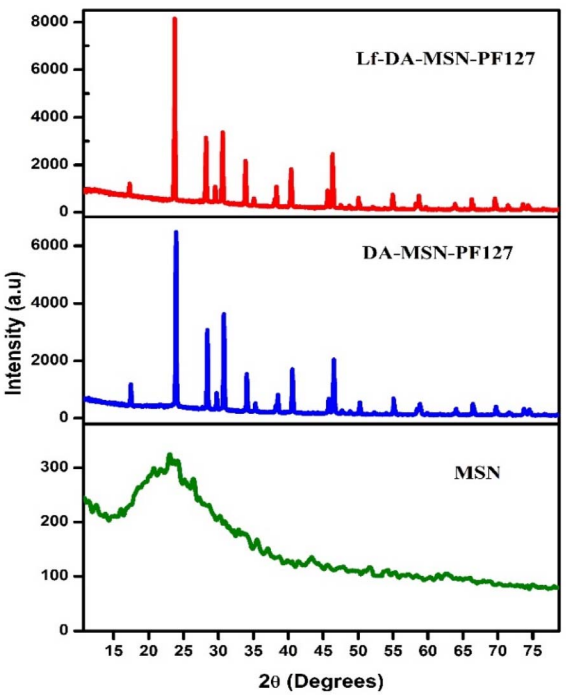

Fig. 3 XRD patterns of MSNs, DA-MSN-PF127 NC, and Lf-DA-MSN-PF127 NC.

bending, respectively. Similar observations were made by Mallinson *et al.*[36] In the FTIR spectrum of DA-MSN, the bands due to both MSN and dopamine were observed with a slight shift in the peak position, which confirms the efficient loading of dopamine into MSN. The FTIR spectrum of PF127 was found to consist of the two bands observed at 2880 and 1100 cm^{-1}, which are characteristic bands for PF127 arising due to oscillation of C–H and C–O groups, which is in good agreement with the results reported by Zanetti *et al.*[37] Furthermore, the bands located at 469, 810, and 1073 corresponded to the MSNs with a slight shift in the band position towards longer wavelengths due to the loading of DA and encapsulation with PF127 in the FTIR spectrum of DA-MSN-PF127. Additionally, this was supported by the peaks positioned at 1289, 1622, and 2923 cm^{-1}, assigned to DA and PF127, respectively. Amide I and amide II are distinctive peaks that may be seen in the FTIR spectrum of lactoferrin. Amide I bands, which are often recognized as being indicative of alpha helices, were located about 1645 and 1649 cm^{-1}. The stretching and bending oscillation of C–N and N–H groups of amides II was characterized by the peaks existing at 1544 and 1536 cm^{-1}. The band located at 3347 cm^{-1} was due to the stretching of peptide N–H.[47,48] The FTIR spectrum of Lf-DA-MSN-PF127 depicted the peaks due to Lf in addition to

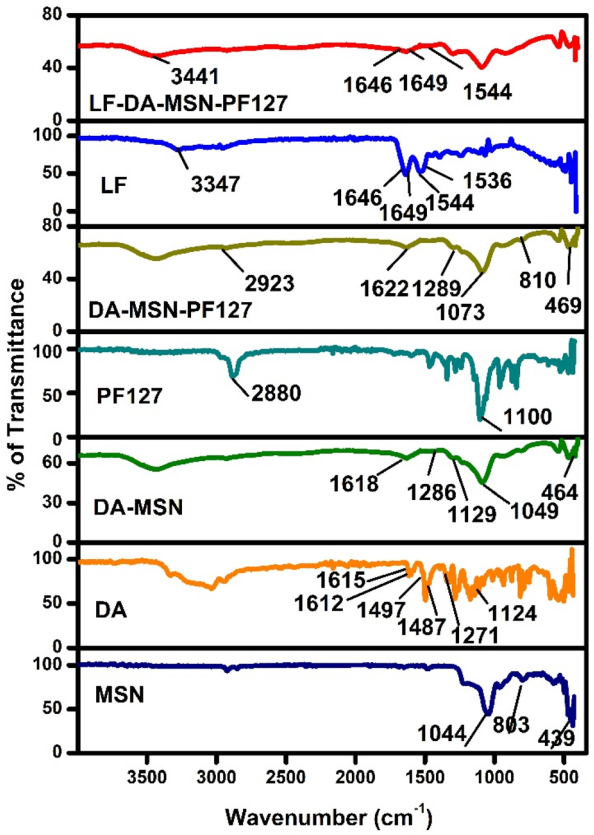

Fig. 4 FTIR spectra of MSNs, DA, DA-MSN, PF127, DA-MSN-PF127 NC, Lf, and Lf-DA-MSN-PF127 NC.

peaks due to DA-MSN-PF127, which ensured the successful conjugation of Lf to DA-MSN-PF127.

The surface morphology of MSNs, DA-MSN-PF127, and Lf-DA-MSN-PF127 was analysed using FE-SEM, and images are depicted in Fig. 5. From Fig. 5A and B, the MSNs were found to be spherical-shaped particles made up of two or more MSN crystals with pores on their surface. This porous morphology could assist in the efficient loading of DA. FE-SEM images of DA-MSN-PF127 (Fig. 5C and D) illustrated the less porous nature of the spherical-shaped MSN particles due to loading DA and encapsulation with PF127. This was further supported by the presence of a bunch of small beads, like particles, which were anchored to MSNs. The FE-SEM images of Lf-DA-MSN-PF127 (Fig. 5E and F) showed a bar-like morphology, which can be compared to a nutted chocolate bar. The presence of these kinds of nutted particles could support the conjugation of lactoferrin to PF127. The EDX spectrum of MSNs (Fig. 5G) illustrated that it consisted of Si and O elements. No other elements were present, which confirms the purity of the synthesised MSNs. The EDX spectrum of DA-MSN-PF127 (Fig. G and H) was found to consist of N, C, H, in addition to Si and O. This confirms the efficacious loading of dopamine and encapsulation with PF127. Furthermore, the EDX spectrum of Lf-DA-MSN-PF127 (Fig. 5I) also showed the presence of Si, O, N, C and H elements only. The decrease in surface area observed in MSN following DA loading and PF127 coating is mainly due to the occupation of internal pores and the formation of a polymer layer on the surface.[38] Several factors contribute to this reduction, including the blocking of MSN by DA, the coating of the MSN external surface by PF127 and strong interactions between DA, PF127 and MSN surface, which can result in strong adsorption. Additionally, the DA-loaded and PF127-coated MSNs exhibit aggregation, further reducing the overall accessible surface area after drug loading and polymer modification.[39]

Fig. 6 shows TEM, HR-TEM and SAED studies performed to determine the internal morphology of the as-prepared MSNs and Lf-DA-MSN-PF127. The TEM image of MSNs (Fig. 6A) was brighter in shade with a spherical shape, whereas the Lf-DA-MSN-PF127 (Fig. 6B) has a darker shade due to loading, unwavering conjugation, and functionalization of DA, PF127 and Lf, respectively. The average particle sizes of MSNs and Lf-DA-MSN-PF127 were found to be 124 and 146 nm, respectively.

HR-TEM images illustrate the ordered arrangement of hexagonal mesosphere. No fringes of sharp spots were seen; instead, a broad, diffuse halo or ring was observed in the SAED pattern (Fig. 6C and F). It illustrates that MSN is amorphous, which is in good agreement with the XRD pattern. The particle sizes measured using DLS were found to be larger than those observed in TEM studies. This discrepancy arises because DLS measures the hydrodynamic diameter, which includes the particle along with its solvent layer, hydration shell, and aggregation effects, impacting colloidal stability. Additionally, DLS provides an average size measurement based on light scattering, whereas TEM captures the actual physical size of individual particles in a dry state.[40]

2.2. Drug loading, entrapment efficiency and *in vitro* drug releasing studies

The DA was loaded into the MSNs by soaking it in phosphate buffer saline at pH 7.4. The loading of DA in MSNs was quantified using the internal standard method, referencing the DA standard calibration curve at $\lambda = 280$ nm. The DA entrapment and loading efficiencies in MSNs were 44.52 ± 2.53 and 24.73 ± 1.40, receptively. The DA released from DA-MSN, DA-MSN-PF127 and Lf-DA-MSN-PF127 was studied for 72 h in phosphate buffer saline (PH 7.4) at 37 ± 1 °C (Fig. 7). The release profile indicates that 91.14 ± 3.20% of DA were released from DA-MSN into PBS within a period of 24 h. However, 79.54 ± 2.94% and 73.23 ± 3.05% of DA were released from DA-MSN-PF127 and Lf-DA-MSN-PF127 respectively, within a period of 72 h.

2.3. *In vivo* blood–brain barrier crossing studies

The evaluation of the BBB crossing ability of DA-MSN-PF127 and Lf-DA-MSN-PF127 was conducted on healthy rats (Fig. 8). Using ICP-OES analysis of MSNs in brain tissue, we quantitatively determined the ability of DA-MSN-PF127 and Lf-DA-MSN-PF127 NC to cross the BBB after intranasal administration at 1, 3, and 9 h time points (Fig. 8A). The bioaccumulation of Si (Silicon) in the rat brain was found to be 4.02 ± 0.65, 11.87 ± 1.31 and 29.08 ± 3.11 μg of Si per g of tissue at 1, 3, and 9 h,

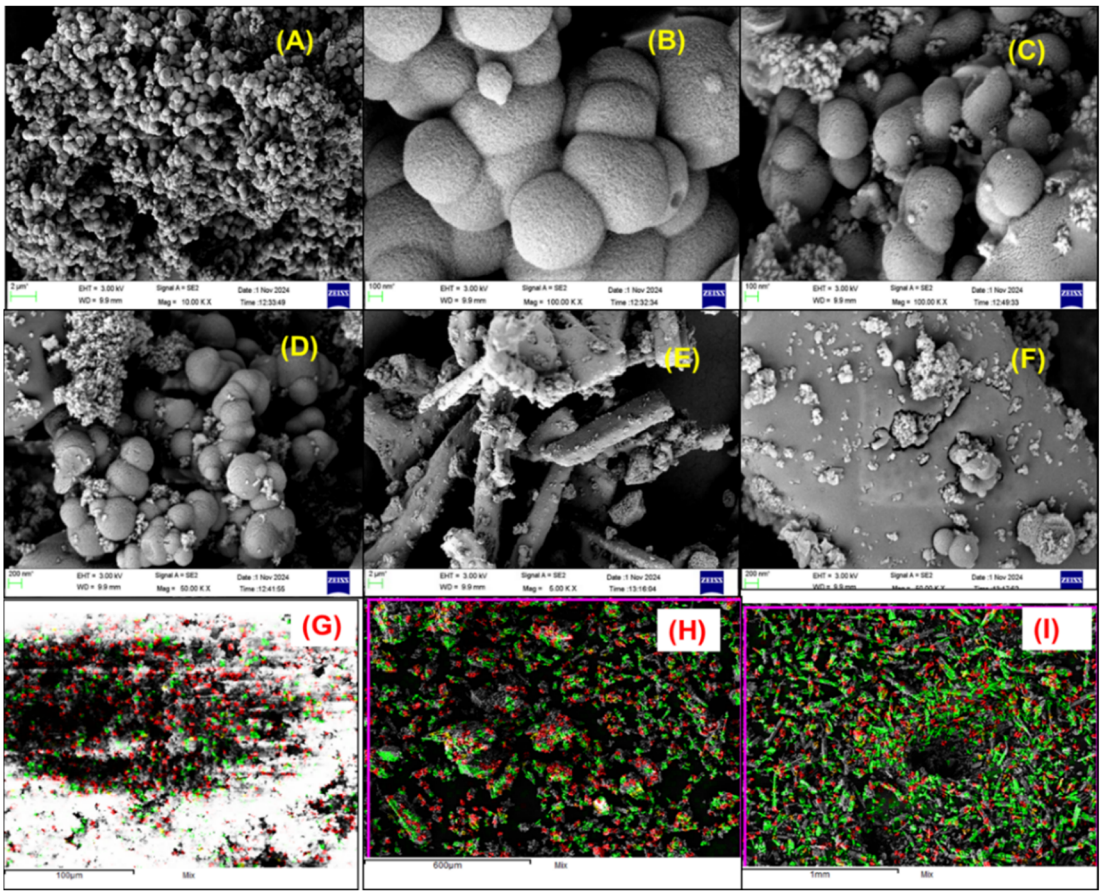

Fig. 5 FE-SEM images of (A and B) MSNs, (C and D) DA-MSN-PF127, and (E and F) Lf-DA-MSN-PF127; elemental mapping of (G) MSNs, (H) DA-MSN-PF127, and (I) Lf-DA-MSN-PF127.

respectively, in the DA-MSN-PF127-treated rat. Similarly, rats administered with Lf-DA-MSN-PF127 showed 7.50 ± 1.04, 26.24 ± 3.16 and 43.08 ± 4.46 μg Si per g of tissue at 1, 3 and 9 h of MSNs. Compared to DA-MSN-PF127 NC, the Lf-DA-MSN-PF127 significantly increased the BBB crossing and bioaccumulation in brain tissue ($F(5, 30) = 126$; $P > 0.001$; Fig. 8A).

To further support the BBB crossing of NC results, the dopamine levels in the brain were determined by the HPLC-ECD. After the intranasal administration of DA-MSN-PF127 and Lf-DA-MSN-PF127 NC at 1, 3 and 9 h, as shown in Fig. 8B, the dopamine levels were found to be significantly increased at 9 h in rats administered Lf-DA-MSN-PF127 ($F(6, 35) = 15.66$; $P > 0.0001$; Fig. 8B) and DA-MSN-PF127 ($F(6, 35) = 15.66$; $P > 0.05$; Fig. 8B) compared to untreated rats.

At 1 and 3 h, the DA-MSN-PF127 treated rats did not show a significant difference in the DA level compared to the control.

However, the Lf-DA-MSN-PF127 NC-treated rats showed a significantly improved DA level at the 3 h time point, compared to control rats ($F(6, 35) = 15.66$; $P > 0.05$; Fig. 8B).

Lf-DA-MSN-PF127 significantly enhances BBB crossing and DA delivery to the brain compared to DA-MSN-PF127 alone. The ICP-OES analysis quantitatively confirmed higher bioaccumulation of Si in the brain tissue at 9 h post-intranasal administration. Similarly, HPLC-ECD showed a significant increase of DA at 9 h in Lf-DA-MSN-PF127-treated rats, demonstrating improved DA delivery. The obtained results suggested the effectiveness of Lf modification in enhancing the brain-targeting capabilities of nanoparticles. Lf-DA-MSN-PF127 facilitates the nasal cavity to the brain *via* a systemic route involving absorption into the bloodstream, followed by transport across the BBB, and a direct route that bypasses the BBB *via* the olfactory nerve.[41] So, Lf and PF127 modified DA-loaded MSNs not only enhance the uptake and transport of DA *via* the nasal mucosa, but also improve the DA by opening the tight junctions of the BBB.[42] Furthermore, Lf receptors (LfR) are overexpressed in age-related neurodegenerative diseases, leading to higher brain uptake compared to other proteins like transferrin.[43] Additionally, Lf serves as a specific ligand for receptor-mediated nasal-to-brain delivery of nanoparticles (NCs) in the intranasal administration of drugs.[22]

Lopalco *et al.*,[44] developed lactoferrin-modified liposomal nanoparticles to enhance dopamine (DA) delivery to the brain, aiming to improve therapeutic outcomes. However, their research was limited to *in vitro* studies. Similarly, Ortega Martínez *et al.*,[45] formulated DA-loaded chitosan-coated solid lipid nanoparticles, but their work was also confined to evaluating blood–brain barrier (BBB) penetration *in vitro*. Monge-Fuentes *et al.*,[5] and Pahuja *et al.*,[46] created DA-loaded polymer

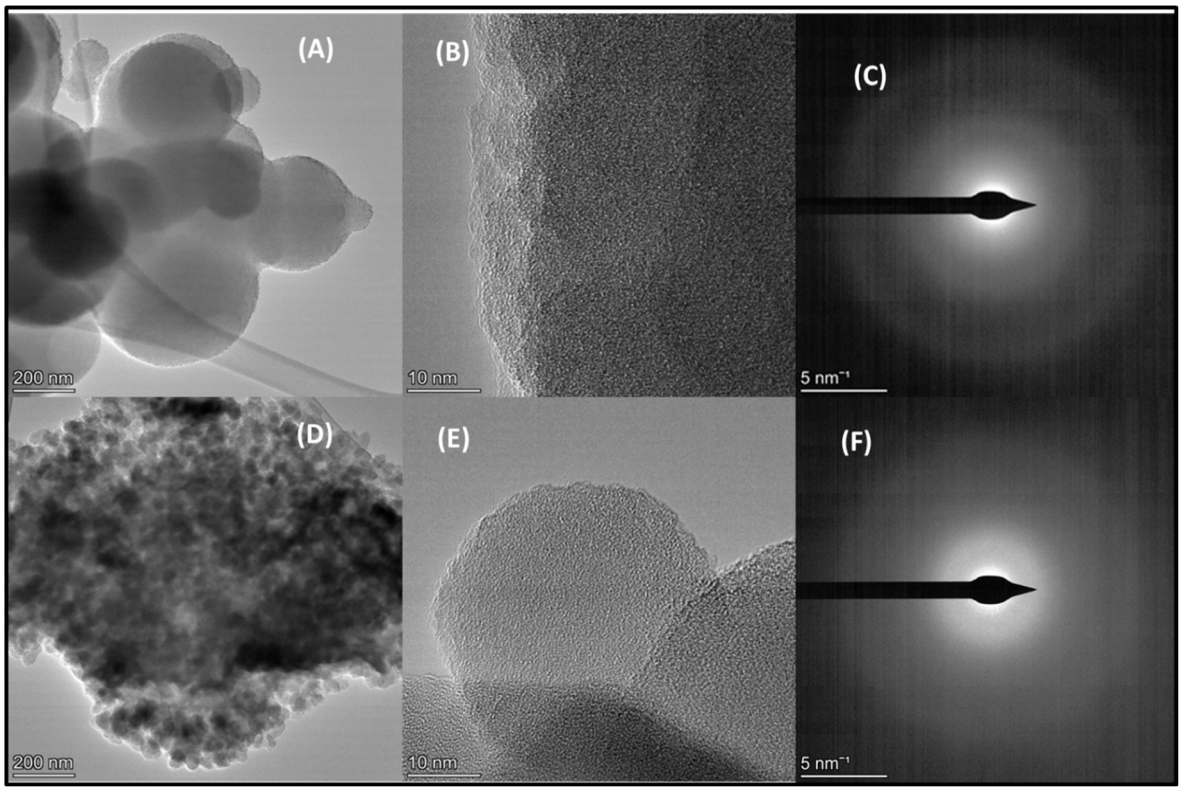

Fig. 6 TEM (A), HR-TEM (B) and selected area electron diffraction (SAED) pattern (C) of MSNs; TEM (D), HR-TEM (E) and selected area electron diffraction (SAED) pattern (F) of Lf-DA-MSN-PF127.

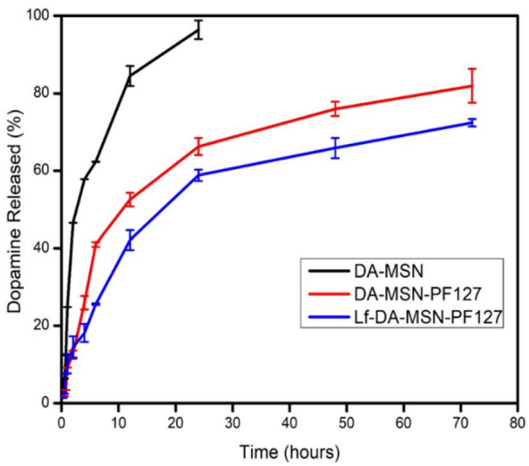

Fig. 7 *In vitro* DA release from DA-MSN, DA-MSN-PF127 and Lf-DA-MSN-PF127 at time points from 0 to 72 h phosphate buffer (PH 4.5).

nanocomposites for effective intravenous delivery to effectively deliver DA to the brain. The intravenous administration of nanoparticles poses challenges, as interactions with blood components can impact nanoparticle stability, circulation time, and biodistribution, thereby reducing therapeutic effectiveness.[47] Additionally, protein binding to nanocarriers may lead to premature drug release.[48] To address these challenges and bypass first-pass metabolism, recent research has focused on intranasal delivery of dopamine (DA) to the brain.[49,50] In this context, S. Tang *et al.*[42] and Q. Guo *et al.*[50] successfully developed *in vivo* delivery of Lf modified DA-loaded NCs for the effective treatment of PD. Corroborating on previous research, the present study demonstrates that Lf-modified DA-MSN-PF127 nanoparticles effectively cross the blood–brain barrier (BBB) and deliver dopamine directly to the brain. This finding highlights the potential of ligand-functionalized nanocarriers in overcoming one of the major challenges in targeted neurotherapeutics.

2.4. Therapeutic effect of Lf-DA-MSN-PF127 on ROT-induced PD rats

Based on *in vivo* BBB crossing studies, we selected Lf-DA-MSN-PF127 for motor and DA level evaluation on ROT-induced PD rats. ROT is a complex I inhibitor of the mitochondrial electron transport chain, and its exposure causes epidemiological PD in humans.[51] ROT triggers several pathogenic pathways in PD by disrupting calcium signalling,[52,53] increasing oxidative stress, apoptosis and reducing tyrosine hydroxylase (TH) levels.[54] This cascade leads to proteasomal dysfunction and iron accumulation in the *substantia nigra*, ultimately resulting in the formation of fibrillary cytoplasmic inclusions that contain ubiquitin and α-synuclein.[55] Furthermore, ROT induces motor and non-motor symptoms that closely resemble those seen in human PD. The narrow beam walking and wire hanging tests are well established tests for assessing the dynamic balance and

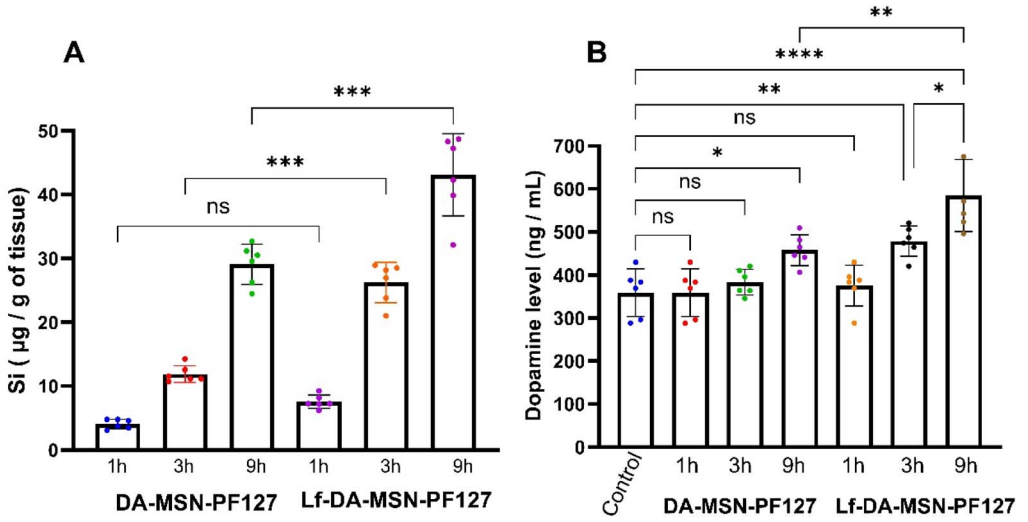

Fig. 8 *In vivo* blood–brain barrier crossing study DA-MSN-PF127 and Lf-DA-MSN-PF127. (A) Time dependent concentrations (µg Si per g brain tissue) of mesoporous silica nanoparticles in normal rat brain tissue. (B) Time-dependent concentrations of DA levels in the normal rat brain. Data are expressed in mean ± SE, significant differences compared to control indicated by *p < 0.05, **p > 0.001, ***p < 0.0001, and ns = no significant; ordinary one-way ANOVA (Tukey's *post hoc* test).

coordination, vestibular integrity, neuromuscular strength, walking, vestibular integrity and impairment of limb movement, in ROT induced animals.[56] In the current study, 2.5 mg kg^{-1} of ROT was administered *via* intraperitoneal injection for 28 days, which did not cause mortality in the ROT-induced group. The used ROT dose in the study has been within a range that induces motor dysfunction without causing fatality. Similarly, the Lf-DA-MSN-PF127-treated group did not cause any mortality, which suggests that the chosen dose is not toxic.

We further evaluated the PD symptoms in ROT-induced rats as shown in Fig. 9 using beam walking and wire hanging tests. ROT induced PD rats showed a significant increase in the time taken to cross the narrow beam ($F(3, 20) = 44.31$; $P > 0.0001$; Fig. 9A) and a reduction in wire hanging time ($F(3, 20) = 53.45$; $P > 0.0001$; Fig. 9B) compared to untreated rats. The ROT induced PD rats' treatment with Lf-DA-MSN-PF127 resulted in a significant decrease in the narrow beam crossing time ($F(3, 20) = 44.31$; $P > 0.05$; Fig. 9A) and a notable increase in wire hanging time ($F(30, 20) = 53.45$; $P > 0.005$; Fig. 9B), compared to the ROT induced PD rats. Additionally, the control group of Lf-DA-MSN-PF127-treated rats did not show any motor impairment compared to control rats.

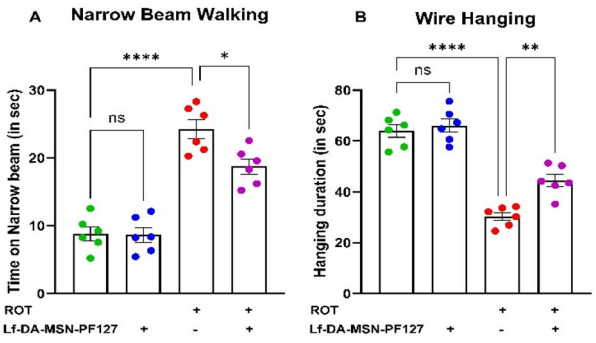

Fig. 9 The effect of Lf-DA-MSN-PF127, ROT, and co-treatment of ROT with Lf-DA-MSN-PF127 for 28 days, on (A) narrow beam test and (B) wire hanging test. Data are expressed in mean ± SE, significant differences compared control indicated by *p < 0.05, **p > 0.001 and ****p < 0.0001; ordinary one-way ANOVA (Tukey's *post hoc* test).

Earlier studies showed that ROT induced behavioral alterations in rats that closely resembled the symptoms of PD in humans.[57] In the present study, we also observed motor symptom impairment in rats induced with ROT, with the increase in narrow beam crossing and decreased wire hanging time. This suggests an induction comparable to what is seen in idiopathic disease and is sensitive to the striatal DA dysfunction. Dopaminergic neurons regulate motor functions and are part of the motor circuit. The ROT influences dopaminergic neurons in the *substantia nigra*, leading to a loss of dopamine, which ultimately results in the impairment of motor functions.[58] The neurobehavioral test results from the current study indicated that DA delivered by Lf-DA-MSN-PF127 enhanced the beam crossing and wire hanging time in comparison to rats with ROT-induced PD.

In comparison to the control group, ROT-induced PD rats exhibited a significant reduction in DA, with a loss of 2.5 times ($F(3, 20) = 42.76$; $P > 0.0001$; Fig. 10). The treatment of Lf-DA-MSN-PF127 with PD-induced rats showed a significant 1.2-fold increase in DA level compared to PD-induced rats ($F(3, 20) = 42.76$; $P > 0.005$; Fig. 10). Compared to the control group, the Lf-DA-MSN-PF127 treatment group exhibited an increased DA level, although the difference was not statistically significant ($F(30, 20) = 42.76$; $p = 0.91$; Fig. 10). DA is a crucial neurotransmitter in the animal kingdom and plays a significant role as a signalling molecule for both motor and non-motor behaviours.[59] Previous studies indicated that intraperitoneal and oral administration of ROT induced progressive loss of dopamine levels in experimental animals and *D. melanogaster*,

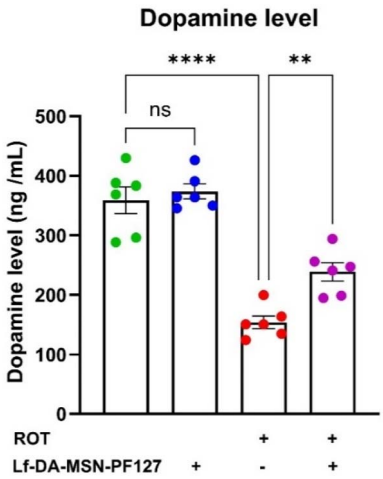

Fig. 10 The effect of Lf-DA-MSN-PF127, ROT and co-treatment of ROT with Lf-DA-MSN-PF127 for 28 days on the dopamine level. Data are expressed in mean ± SE, significant differences compared control indicated by *$p < 0.05$, **$p > 0.001$ and ****$p < 0.00001$; ordinary one-way ANOVA (Tukey's *post hoc* test).

respectively.[60–62] In the present study, we also observed similar results. Oxidative stress induced by ROT causes mitochondrial dysfunction, which leads to progressive loss of dopaminergic neurons and finally decreases the DA synthesis.[52] In the present study, we successfully restored the dopamine (DA) levels reduced by rotenone with the use of Lf-DA-MSN-PF127, confirming its delivery across the BBB. The results also provide evidence that Lf-DA-MSN-PF127 significantly enhanced the ability of DA to cross the BBB. The obtained results corroborated that nasal administration of DA crosses the BBB and increases the DA level, as observed in previous results.[42]

In nanomedicine, ensuring biocompatibility is essential for the effective clinical implementation of nano-therapeutics. In this context, we assess the pathological alterations in the nasal cavity and brain after treatment with ROT and Lf-DA-MSN-PF127 at 28 days (Fig. 11). The results obtained from H&E staining showed that the intraperitoneal administration of ROT caused moderate neuronal degeneration in the brain (Fig. 11A–C), while the intranasal administration of Lf-DA-MSN-PF127 did not cause any damage or significant pathological changes in the brain. Furthermore, Lf-DA-MSN-PF127 did not cause any harm to either the right or left nasal cavity (Fig. 12A and B).

3 Experimental

3.1. Materials

Ammonium hydroxide solution (CAS No. 1336-21-6), 3-aminopropyl triethoxysilane (CAS No. 919-30-2), dopamine hydrochloride (CAS No. 62-37-7), ECD (CAS No. 62-37-7), cetyltrimethylammonium bromide (CTAB; CAS No. 57-09-0), 1-ethyl-3-(3-dimethylaminopropyl)carbodiimide (EDC; 99–102%; CAS No. 25962-53-8), *N*-hydroxy succinimide (NHS; 97–103%; CAS No. 6066-82-6), sodium hydroxide (NaOH; CAS No. 1310-73-2), ammonium acetate, HPLC grade (CAS No. 631-61-8), ethylenediaminetetraacetic acid (EDTA; CAS No. 6281-92-6), citric acid (CAS No. 5949-29-1), 3-(4,5-dimethylthiazol-2-yl)-2,5-diphenyltetrazolium bromide (MTT); antibiotic antimitotic solution 100× liquid (A002A-20ML), Dulbecco's Modified Eagle Medium (DMEM; AL0078-500ML), and Fetal Bovine Serum (FBS; RM1112-500ML) were purchased from HIMEDIA Laboratories Private Limited in India. Methanol (CAS No. 67-56-1) was purchased from the Statutory Liquidity Ratio (SLR) in India. All chemicals were of reagent grade and used as received and stored according to the manufacturer's guidelines. All the aqueous solutions were prepared using Millipore and double-distilled water.

3.2. Synthesis of MSNs

The MSNs were synthesized using the method described by Singh *et al.*,[63] using the 2-methoxy ethanol emulsion method. Briefly, 1 g of cetyltrimethylammonium bromide (CTAB) was dissolved in a mixture of 200 mL of ethanol, 2-ethoxyethanol, and ammonia solution (16 : 4 : 4 volume ratio) and stirred for 30 min at room temperature. 1.5 mL of tetraethyl orthosilicate was added dropwise to the reaction mixture and stirring was continued for 4 h. White coloured MSNs were centrifuged at 10 000 rpm for 30 min and washed with water and ethanol. The sample was further dried at 80 °C and calcined at 600 °C for 4 h for the removal of impurities, if any.

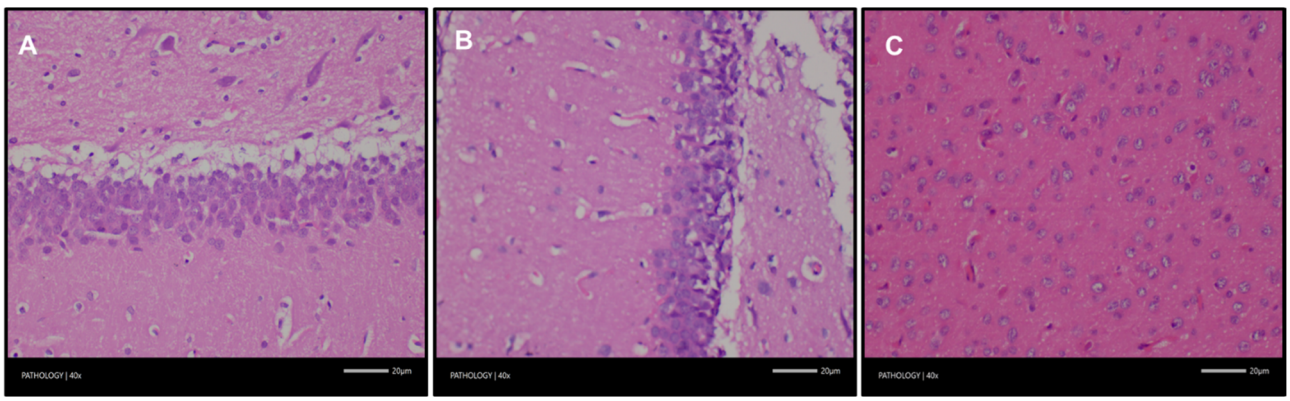

Fig. 11 Histological examination of brain tissue morphology from various treatment groups: control (A), Lf-DA-MSN-PF127 treated (B), and ROT treated (C) brain. The tissue sections were analyzed using hematoxylin and eosin (H&E) staining.

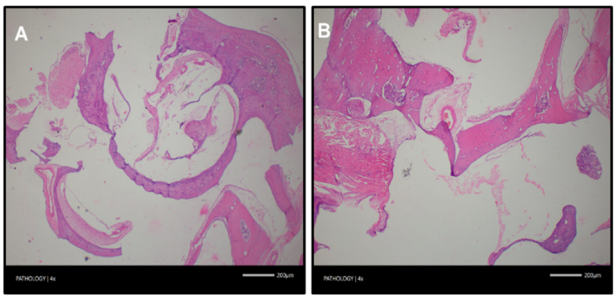

Fig. 12 Histological evaluation of nasal cavity tissue morphology across treatment groups. Representative images are shown for (A) control and (B) Lf-DA-MSN-PF127 treated groups. Tissue sections were stained with hematoxylin and eosin (H&E).

3.3. Synthesis of dopamine-loaded MSNs

Dopamine hydrochloride was loaded into the MSNs based on the method described by So and Wei *et al.*,[64] and Lopalco *et al.*,[65] with some minor modifications. Briefly, 50 mg of dopamine hydrochloride (DA) was dissolved in 10 mL of 0.1 M phosphate buffer (pH 4.5), and 100 mg of MSNs was added. The mixture was stirred for 8 h in the dark. 50 μL of APTES was added and stirred for 4 h at room temperature for amino group modification on the surface of DA-MSN. Furthermore, the DA-loaded MSN was centrifuged at 5000 rpm for 30 min and lyophilized to obtain DA-MSN.

3.4. Synthesis of Pluronic F-127 capped DA-MSN

The capping on the surface of PF-127 to DA-MSN was performed based on the method described by Heggannavar *et al.*[66] In brief, 40 mg of modified PF-127, 52 mg of NHS and 90 mg of EDC were dissolved in 5 mL of phosphate buffer pH 4.5 and stirred for 6 h. Furthermore, amino functionalized DA-MSN (1 mg mL^{-1} of phosphate buffer pH 4.5) was added to the reaction mixture and stirred at 150 rpm for 48 h. The resulting DA-MSN-PF127 was washed several times with phosphate buffer and centrifuged at 5000 rpm for 30 min, freeze-dried, and stored at 4 °C.

3.5. Synthesis of lactoferrin functionalized DA-MSN-PF127

To functionalize the lactoferrin (Lf) to DA-MSN-PF127, 10 mg of DA-MSN-PF127 was dispersed in 5 mL of phosphate buffer (pH 4.5) containing 0.25 mL of EDC and NHS (1 mg mL^{-1}), and the mixture was stirred for 3 h. To this mixture, 200 μL of Lf (1 mg mL^{-1}) was added and stirred for 2 h. Finally, the reaction mixture was incubated for 12 h at 4 °C. The obtained Lf-DA-MSN-PF127 was collected by centrifugation, washed with phosphate buffer (pH 4.5), and finally, the nanocomposite was lyophilized and stored at 4 °C.[65,66]

3.6. Drug loading and entrapment efficiency

The DA loading and entrapment efficiency were determined by using HPLC. The DA-MSN was centrifuged at 5000 rpm for 30 min, and the supernatant obtained was used to assess the loaded DA level. The obtained supernatant was filtered using a 0.2 μm syringe filter, and 20 μL of the filtered supernatant was injected into the HPLC system with a C-18 column (4.6 × 250 mm, 5 μm particle size; Shimadzu Shim-pack). The mobile phase consisted of 0.020 M potassium phosphate buffer (pH 2.5) and acetonitrile in a 90 : 10 (v/v) ratio, and the analysis was conducted in isocratic mode. The flow rate was maintained 1 mL min^{-1} for 10 min. The DA peak was identified at 280 nm and quantified using an LD standard calibration curve ($r^2 = 1$; Fig. S1). The loading and entrapment efficiency were determined by using the following formula.[46]

$$\text{Loading efficiency}(\%) = \frac{\text{weight of DA in MSN}}{\text{total weight of MSN}} \times 100$$

$$\text{Entrapment efficiency}(\%) = \frac{\text{weight of DA in MSN}}{\text{weight of total DA}} \times 100$$

3.7. Characterization of the nanocomposite

UV-Visible Diffuse Reflectance Spectroscopy (Labindia UV-3090; Chloros Energy Material Characterization Centre, Tumkuru, India) was used to analyse the optical properties of the prepared MSNs, DA-MSN, DA-MSN-PF127, and Lf-DA-MSN-PF127. The nitrogen adsorption–desorption isotherms were used to evaluate the pore size distribution and surface area of the synthesised MSNs using the BET surface area analyser (BEL JAPAN-Japan; Vijnana Bhavan, Manasagangotri, University of Mysore, Mysuru). The FTIR studies of DA, Lf, PF127, DA-MSN, DA-MSN-PF127, and Lf-DA-MSN-PF127 were carried out using Shimadzu (Chloros Energy Material Characterization Centre, Tumkuru, India). The phase purity and crystallinity of the MSNs, DA-MSN-PF127, and MSN-DA-MSN-PF127 were evaluated through XRD patterns by using a Bruker D8 ADVANCE (Chloros Energy Material Characterization Centre, Tumkuru, India). The synthesised MSNs, DA-MSN-PF127, and Lf-DA-MSN-PF127 were characterized for their shape and surface morphology by using FE-SEM (Carl Zeiss, Germany, Model SUPRA 55). The elemental composition and purity of the prepared nanomaterials were acquired by using an Oxford instrument energy-dispersive spectrophotometer, UK, Germany (Chloros Energy Material Characterization Centre, Tumkuru, India). A transmission electron microscope (TEM) on JEOL JEM 2100 PLUS was used to detect the morphology of DA-MSN-PF127 and Lf-DA-MSN-PF127 (Chloros Energy Material Characterization Centre, Tumakuru, India). The zeta potential, vesicle dimension, and polydispersity index (PDI) of MSNs, DA-MSN-PF127, and Lf-DA-MSN-PF127 were determined using a dynamic light scattering HORIBA scientific, SZ-100, Ver2.20 (University Science Instrumentation Facility phase-II, Karnatak University, Dharwad, India).

3.8. *In vitro* drug release study

The *in vitro* drug release assay was carried out based on the method described by Lopalco *et al.*,[65] and Pahuja *et al.*,[46] using the dialysis method. Briefly, 10 mg of DA-MSN, DA-MSN-PF127, and Lf-DA-MSN-PF127 each were dispersed in 3 mL of phosphate buffer saline (pH 7.4) and placed into separate dialysis membranes (Spectra/Por®; Molecular cut-off, 12–14 kDa). The membrane was

allowed to dialyze against 50 mL of phosphate buffer saline (pH 7.4) containing 0.005 α-tocopherol, at 37 °C in a shaker incubator (Lab Companion; SIF6000R). At different time intervals, 1 mL of buffer was withdrawn and replaced with an equal volume of fresh buffer. The samples were analysed at 280 nm using a UV-Visible spectrophotometer, and the amount of released DA was calculated using a DA calibration curve ($r^2 = 0.998$; Fig. S2).

3.9. Animals

Adult male SD rats of ten to eleven days old (190–200 g) were procured from Chromed Biosciences Pvt. Ltd, Tumkur, Karnataka, India, and were kept under a 12 hour light/dark cycle at a temperature of 25 ± 2 °C, with free access to food and water. The animals were acclimatized for a week before the study. The handling and experimentation were approved by the Institutional Animal Ethics Committee (IAEC), Chromed Biosciences Pvt. Ltd, India (Approval number CBPL-IAE-096/10/2024).

3.10. *In vivo* BBB penetration of Lf-DA-MSN-PF127 and DA-MSN-PF127

The BBB crossing of Lf-DA-MSN-PF127 and DA-MSN-PF127 was analysed in healthy Sprague-Dawley rats based on a method described by Bao *et al.*,[67] and Wang *et al.*,[68] with some modifications. Both Lf-DA-MSN-PF127 and DA-MSN-PF127 were dispersed in saline separately and were injected into two groups *via* the intranasal (i.n.) route. After the predominant time interval (1 h, 3 h, and 9 h), rats were deeply anaesthetised through isoflurane inhalation, dissected, and the brain was excised and weighed. The brain samples were digested in a microwave oven under the conditions of 1600 W and 190 °C for 2 h, and used for measuring the concentration of Si using ICP-OES. The brain tissue homogenate was used further to determine the DA level using HPLC-ECD.[60,69]

3.11. Therapeutic effect of Lf-DA-MSN-PF127 on the ROT-induced PD rat model

3.11.1. Treatment. 50 mg of ROT was dissolved in 1 mL of DMSO and then diluted in sunflower oil to obtain a final concentration of 2.5 mg mL^{-1} (2.5 μg μL^{-1}). Each time, freshly prepared ROT was used for all the experiments.[70]

After five days of acclimatization, rats were divided into four groups of twelve rats in each group: (a) control group injected with normal saline once a day for 28 days ($n = 12$), (b) second group of rats received daily single intranasal (i.n.) dose of Lf-DA-MSN-PF127 (equivalent to 5 mg per kg weight of DA) ($n = 12$)[71] for 28 days, (c) third group of rats received daily intraperitoneal (i.p.) injections of ROT for 28 days (2.5 mg kg^{-1}) ($n = 12$)[70,72,73] and (d) the fourth group of rats were administered a single intranasal (i.n.) dose of Lf-DA-MSN-PF127 (equivalent to 5 mg per kg weight of DA)[71] ($n = 12$), 30 minutes after an intraperitoneal (i.p.) injection of ROT (2.5 mg kg^{-1}), for 28 days.

Motor impairment tests were carried out on the 28th day. Following the behavioural assessment on the 28th day, the rats were sacrificed, and brain tissues were collected for measuring dopamine levels. Additionally, both the brain and nose tissues were collected for histopathological evaluation.

3.11.2. Behavioural assay. To assess motor impairment, narrow beam and wire hanging assays were performed following the methods outlined by Kumar *et al.*,[74] and Tseng *et al.*,[75] respectively. For the narrow beam assay, rats were permitted to walk on a flat wooden beam (8 cm in diameter, 0.5 mm in thickness, 2 cm in width, and 120 cm in length), which was placed 50 cm above the ground. The time taken by each rat to move from one end of the beam to the other was recorded, and the average time was calculated after testing each rat six times independently. For the wire hanging assay, rats were allowed to hold their forelimbs on a 90 cm length and 3 mm diameter stainless steel wire mounted between two platforms at above 60 cm above the ground. The time it takes for mice to fall off the wire was recorded; each mouse was tested in six independent trials, and the average time was calculated for analysis.

3.11.3. Homogenate preparation for HPLC-CED. The brain tissue was homogenised with 0.2 N perchloric acid and centrifuged at 10 000 rpm (REMI Cooling Centrifuge C-24 BL) for 10 min at 4 °C. Furthermore, it was filtered through a 0.2 μm syringe (AXIVA syringe filter nylon-13 mm/0.2 μm), and the filtrate was used for HPLC-ECD.

3.11.4. Determination of the dopamine level. The DA level was determined using the method described by Hanumanthappa *et al.*,[76] and Smruthi *et al.*,[69] using HPLC-ECD. Briefly, 20 μL of filtered sample was injected into the HPLC system (C-18 column: Spherisorb, RP C18, 5 μm particle size, 4 mm × 250 mm at 30 °C; electrochemical detector: model 1645, Waters, USA). The mobile phase consists of 17.6% methanol and 82.4% water and consists of 0.0876 mM of EDTA, 1.5 mM of TEA, 9 mM of DL-$C_{10}H_{16}O_4S$, 20 mM Na_2HPO_4, and 15 mM citric acid (pH 4.2). It was pumped at a flow rate of 1.5 mL min^{-1}. The DA concentration in the sample was analysed by comparing it with the standard peak area (Fig. S3) and expressed as ng g^{-1} of tissue.

3.11.5. Histopathology. After the rats were sacrificed, the brain and nose samples were collected and fixed in 10% buffered formalin. The tissue was processed using a TP 1020 Leica Germany automated tissue processing. Furthermore, paraffin-embedded (HistoCore Arcadia H) samples were subsequently sliced into 4 μm thickness using a microtome (Leica RM2125 RTS, Germany) and stained with Haematoxylin and Eosin (H&E). Histological assessment was performed under a light microscope (OLYMPUS CX33, Japan) to evaluate the potential toxicity of Lf-DA-MSN-PF127.

3.12. Data analysis

The Graph Pad Prism 10.2.3 software was used for statistical analysis and plotting graphs; for ordinary one-way ANOVA (Tukey's *post hoc* test) of mean ± SE, for $n = 6$, significant differences compared to control were indicated by $*p < 0.05$, $**p > 0.001$, and $***p < 0.0001$.

4 Conclusions

For the management of PD, the successful delivery of DA to the brain, overcoming the BBB challenge, is crucial. The CNS-targeted Lf-modified nanoparticles could provide a strategy to

address these challenges. The current study demonstrated that Lf-DA-MSN-PF127 enhanced BBB crossing and dopamine delivery in rats, compared to DA-MSN-PF127. Furthermore, the treatment of the ROT-induced PD rat model with Lf-DA-MSN-PF127 improved motor function and restored dopamine levels. Histological analysis confirmed the biocompatibility of Lf-DA-MSN-PF127, with no damage to the brain or nasal cavity. Additionally, MSNs, Lf-DA-MSN-PF127, and Lf-DA-MSN-PF127 did not show significant toxicity on the SHY-SY5Y cell line. The study demonstrates that the Lf-DA-MSN-PF127 nanocomposite delivers DA to the brain, offering a therapeutic approach for managing motor symptoms and DA levels in PD. It appears to be a promising treatment option.

Declaration

The figures presented in this manuscript are original in nature and were produced from the raw data generated by the authors on their own. None of the figures were borrowed from previous studies.

Author contributions

Conceptualization – Kuramkote Shivanna Devaraju, Hemalatha Nanjaiah and Ramesha Hanumanthappa; methodology – Ramesha Hanumanthappa and Sumit Ramesh Naik; investigation – Kuramkote Shivanna Devaraju and Ramesha Hanumanthappa; writing original draft – Ramesha Hanumanthappa; writing review & editing – Nethravathi P. C.; software – Ramesha Hanumanthappa and Sahana Prakash Naik; data curation – Kuramkote Shivanna Devaraju, Raghu S. V., D. Suresh, Hemalatha Nanjaiah and Asmatanzeem Bepari; supervision – Kuramkote Shivanna Devaraju; validation – Kuramkote Shivanna Devaraju, Raghu S. V., D. Suresh and Hemalatha Nanjaiah; formal analysis – Hanan Nasser Altamimi, Mujeeb Ahmed Shaikh, Fahd A. Nasr and Farha M. Shaikh. All authors read and approved the final manuscript.

Conflicts of interest

There are no conflicts to declare.

Data availability

The data supporting this article have been included as part of the SI. Raw data are also accessible from the corresponding author (Kuramkote Shivanna Devaraju) upon reasonable request.

Fig. S1 and S2: Standard curve by HPLC-UV detector and UV-Visible spectrophotometer of dopamine respectively; Fig. S3, S4, S5, S6, S7 and S8: FITR spectra of MSN, DA, PF127, DA-MSN-PF 127, Lf and Lf-DA-MSN-PF127 respectively; Fig. S9: Nitrogen gas adsorption–desorption isotherms for MSN NPs and Fig. S10: Pore size distribution obtained from adsorption measurements; Table S1: UV-DRS of MSN, DA-MSN, DA-MASN-PF127 and Lf-DA-MASN-PF127 of UV-DRS. See DOI: **https://doi.org/10.1039/d5na00593k**.

Acknowledgements

The authors acknowledge Chromed Biosciences Private Limited, Tumkuru, India, for providing the lab specialty to conduct the animal study. The authors sincerely acknowledge DFRL Mysore for providing the HPLC-ECD facility; the authors acknowledge Eureka Analytical Services Pvt. Ltd, Bangalore, Karnataka, for providing the ICP-OES facility; the authors sincerely acknowledge Chloros Energy Material Characterization Centre Tumkuru for providing the essential instrumentation services for the characterization of nanocomposites. The authors acknowledge Karnatak University, Dharwad for providing the necessary facilities. This work was supported by Princess Nourah bint Abdulrahman University Researchers Supporting Project (PNURSP2025R105), Princess Nourah bint Abdulrahman University, Riyadh, Saudi Arabia.

References

1 Y. Sun, Digital Biomarkers for Precision Diagnosis and Monitoring in Parkinson's Disease, *npj Digit. Med.*, 2024, **7**, 218.
2 Z. D. Zhou, L. X. Yi, D. Q. Wang, T. M. Lim and E. K. Tan, Role of Dopamine in the Pathophysiology of Parkinson's Disease, *Transl. Neurodegener.*, 2023, **12**(1), 44.
3 A. Islam, L. Alcock, K. Nazarpour, L. Rochester and A. Pantall, Effect of Parkinson's Disease and Two Therapeutic Interventions on Muscle Activity during Walking: A Systematic Review, *npj Parkinson's Dis.*, 2020, **6**(1), 22.
4 D. J. Surmeier, Determinants of Dopaminergic Neuron Loss in Parkinson's Disease, *FEBS J.*, 2018, **285**(19), 3657–3668.
5 V. Monge-Fuentes, A. Biolchi Mayer, M. R. Lima, L. R. Geraldes, L. N. Zanotto, K. G. Moreira, O. P. Martins, H. L. Piva, M. S. S. Felipe, A. C. Amaral, A. L. Bocca, A. C. Tedesco and M. R. Mortari, Dopamine-Loaded Nanoparticle Systems Circumvent the Blood–Brain Barrier Restoring Motor Function in Mouse Model for Parkinson's Disease, *Sci. Rep.*, 2021, **11**(1), 15185.
6 L. B. Vong, Y. Sato, P. Chonpathompikunlert, S. Tanasawet, P. Hutamekalin and Y. Nagasaki, Self-Assembled Polydopamine Nanoparticles Improve Treatment in Parkinson's Disease Model Mice and Suppress Dopamine-Induced Dyskinesia, *Acta Biomater.*, 2020, **109**, 220–228.
7 R. Hanumanthappa, G. B. Heggannavar, A. Banakar, D. D. Achari, V. Ramesh Karoshi, B. R. R. Krushna, A. Bepari, R. Assad Assiri, H. Nasser Altamimi, H. Nanjaiah, D. Sannaningaiah, S. V. Raghu, V. Kaveeshwar, H. Nagabhushana and K. S. Devaraju, A Levodopa-Encapsulated Poly-ε-Caprolactone Nanocomposite Improves the Motor Symptoms and Neurochemical Changes in a Rotenone-Induced Mouse Model of Parkinson's Disease, *ACS Omega*, 2025, **10**, 19682–19696.
8 J. Zhu and M. Chen, The Effect and Safety of Ropinirole in the Treatment of Parkinson Disease: A Systematic Review and Meta-Analysis, *Medicine*, 2021, **100**(46), e27653.

9 R. Constantinescu, Update on the Use of Pramipexole in the Treatment of Parkinson's Disease, *Neuropsychiatr. Dis. Treat.*, 2008, 337.
10 J. C. Morgan and K. D. Sethi, Rotigotine for the Treatment of Parkinson's Disease, *Expert Rev. Neurother.*, 2006, **6**(9), 1275–1282.
11 S. Habet, Clinical Pharmacology of Entacapone (Comtan) From the FDA Reviewer, *Int. J. Neuropsychopharmacol.*, 2022, **25**(7), 567–575.
12 M. Fabbri, J. J. Ferreira, A. Lees, F. Stocchi, W. Poewe, E. Tolosa and O. Rascol, Opicapone for the Treatment of Parkinson's Disease: A Review of a New Licensed Medicine, *Mov. Disord.*, 2018, **33**(10), 1528–1539.
13 L. Nayak and C. Henchcliffe, Rasagiline in Treatment of Parkinson's Disease, *Neuropsychiatr. Dis. Treat.*, 2008, **4**(1), 23–32.
14 K. Kawabata and M. Katsuno, Trihexyphenidyl, Biperiden, and Other Anticholinergics in the Treatment of Parkinson's Disease, in *NeuroPsychopharmacotherapy*, ed. P. Riederer, G. Laux, T. Nagatsu, W. Le and C. Riederer, Springer International Publishing, Cham, 2021, pp. 1–8.
15 R. Hanumanthappa, A. Parthasarathy, G. B. Heggannavar, P. C. Kiran, H. Nanjaiah, R. Kumbhar and K. S. Devaraju, Recent Advances in Therapeutic Strategies for Alzheimer's and Parkinson's Disease Using Protein/Peptide Co-modified Polymer Nanoparticles, *Neuroprotection*, 2024, **2**, 255–275.
16 M. Kahana, A. Weizman, M. Gabay, Y. Loboda, H. Segal-Gavish, A. Gavish, Y. Barhum, D. Offen, J. Finberg, N. Allon and M. Gavish, Liposome-Based Targeting of Dopamine to the Brain: A Novel Approach for the Treatment of Parkinson's Disease, *Mol. Psychiatry*, 2021, **26**(6), 2626–2632.
17 D. Wu, Q. Chen, X. Chen, F. Han, Z. Chen and Y. Wang, The Blood–Brain Barrier: Structure, Regulation, and Drug Delivery, *Signal Transduction Targeted Ther.*, 2023, **8**(1), 217.
18 R. Heidari, P. Khosravian, S. A. Mirzaei and F. Elahian, siRNA Delivery Using Intelligent Chitosan-Capped Mesoporous Silica Nanoparticles for Overcoming Multidrug Resistance in Malignant Carcinoma Cells, *Sci. Rep.*, 2021, **11**(1), 20531.
19 E. İspir, M. İnal, Z. Gün Gök and M. Yiğitoğlu, Synthesis, Characterization and in Vitro Release Analysis of Pluronic F127 Copolymer Micelles Containing Quercetin as a Hydrophobic Drug, *Polym. Bull.*, 2024, **81**(8), 6801–6822.
20 S. Castellani, R. Mallamaci, E. De Giglio, A. Caponio, L. Guerra, G. Fracchiolla, G. Trapani, K. Kristan, R. A. Cardone, G. Passantino, N. Zizzo, G. Franzino, D. Larobina, A. Trapani and M. Conese, Slightly Viscous Dispersions of Mucoadhesive Polymers as Vehicles for Nasal Administration of Dopamine and Grape Seed Extract-Loaded Solid Lipid Nanoparticles, *Int. J. Pharm.*, 2024, **659**, 124255.
21 H. Kim, B. Choi, S. K. Mouli, H. Choi, K. R. Harris, L. M. Kulik, R. J. Lewandowski and D. Kim, Preclinical Development and Validation of Translational Temperature Sensitive Iodized Oil Emulsion Mediated Transcatheter Arterial Chemo-Immuno-Embolization for the Treatment of Hepatocellular Carcinoma, *Adv. Healthcare Mater.*, 2023, **12**(26), 2300906.
22 Z. Liu, M. Jiang, T. Kang, D. Miao, G. Gu, Q. Song, L. Yao, Q. Hu, Y. Tu, Z. Pang, H. Chen, X. Jiang, X. Gao and J. Chen, Lactoferrin-Modified PEG-Co-PCL Nanoparticles for Enhanced Brain Delivery of NAP Peptide Following Intranasal Administration, *Biomaterials*, 2013, **34**(15), 3870–3881.
23 X. Cao, Y. Ren, Q. Lu, K. Wang, Y. Wu, Y. Wang, Y. Zhang, X. Cui, Z. Yang and Z. Chen, Lactoferrin: A Glycoprotein That Plays an Active Role in Human Health, *Front. Nutr.*, 2023, **9**, 1018336.
24 Y. A. Suzuki, V. Lopez and B. Lönnerdal, Lactoferrin: Mammalian Lactoferrin Receptors: Structure and Function, *Cell. Mol. Life Sci.*, 2005, **62**(22), 2560–2575.
25 L. Zecca, M. B. H. Youdim, P. Riederer, J. R. Connor and R. R. Crichton, Iron, Brain Ageing and Neurodegenerative Disorders, *Nat. Rev. Neurosci.*, 2004, **5**(11), 863–873.
26 C. Malba, U. P. Sudhakaran, S. Borsacchi, M. Geppi, F. Enrichi, M. M. Natile, L. Armelao, T. Finotto, R. Marin, P. Riello and A. Benedetti, Structural and Photophysical Properties of Rare-Earth Complexes Encapsulated into Surface Modified Mesoporous Silica Nanoparticles, *Dalton Trans.*, 2014, **43**(43), 16183–16196.
27 N. O. A. Al-Salahi, E. Y. Hashem and D. A. Abdel-Kader, Spectrophotometric Methods for Determination of Dopamine Hydrochloride in Bulk and in Injectable Forms, *Spectrochim. Acta, Part A*, 2022, **278**, 121278.
28 R. A. Almaimani, Synthesis and Characterization of Pluronic F-127-Coated Titanium Dioxide Nanoparticles Synthesized from Extracts of *Atractylodes Macrocephala* Leaf for Antioxidant, Antimicrobial, and Anticancer Properties, *Green Process. Synth.*, 2023, **12**(1), 20230100.
29 P. Xue, H. Zhao, X. You and W. Yue, Structural and in Vitro Anticancer Properties of the Kaempferol–Lactoferrin Complex, *Food Sci. Nutr.*, 2024, **12**, 9046–9055.
30 A. Sadeghi, S. PourEskandar, E. Askari and M. Akbari, Polymeric Nanoparticles and Nanogels: How Do They Interact with Proteins?, *Gels*, 2023, **9**(8), 632.
31 A. Cartwright, K. Jackson, C. Morgan, A. Anderson and D. W. Britt, A Review of Metal and Metal-Oxide Nanoparticle Coating Technologies to Inhibit Agglomeration and Increase Bioactivity for Agricultural Applications, *Agronomy*, 2020, **10**(7), 1018.
32 F. Mahfoozi, A. Mahmoudi, M. R. Sazegar and K. Nazari, High-Performance Photocatalytic Degradation of Neutral Red over Cobalt Grafted-Mesoporous Silica under UV Irradiation, *J. Sol-Gel Sci. Technol.*, 2021, **100**(1), 170–182.
33 R. Meng, Y. Chen, X. Zhang, X. Dong, H. Ma and G. Wang, Synthesis of a Hydrophilic α-Sulfur/PDA Composite as a Metal-Free Photocatalyst with Enhanced Photocatalytic Performance under Visible Light, *J. Macromol. Sci., Part A:Pure Appl. Chem.*, 2017, **54**(5), 334–338.
34 D. Marinheiro, B. Ferreira, P. Oskoei, H. Oliveira and A. Daniel-da-Silva, Encapsulation and Enhanced Release of

Resveratrol from Mesoporous Silica Nanoparticles for Melanoma Therapy, *Materials*, 2021, **14**(6), 1382.

35 X. Wen, Z. Xiao, T. Jiang, J. Li, W. Zhang, L. Zhang and H. Shao, Constructing Novel Fiber Reinforced Plastic (FRP) Composites through a Biomimetic Approach: Connecting Glass Fiber with Nanosized Boron Nitride by Polydopamine Coating, *J. Nanomater.*, 2013, **2013**(1), 470583.

36 D. Mallinson, A. B. Mullen and D. A. Lamprou, Probing Polydopamine Adhesion to Protein and Polymer Films: Microscopic and Spectroscopic Evaluation, *J. Mater. Sci.*, 2018, **53**(5), 3198–3209.

37 M. R. L. Zanetti, A. M. Percebom, T. A. Ribeiro, M. L. Dias, A. P. Oliveira, E. R. Júnior, A. L. Rossi, C. A. G. Soares and P. H. S. Picciani, Improving in Vitro Biocompatibility of Gold Nanorods with Thiol-Terminated Triblock Copolymer, *Colloid Polym. Sci.*, 2019, **297**(11–12), 1477–1487.

38 F. Rizzi, R. Castaldo, T. Latronico, P. Lasala, G. Gentile, M. Lavorgna, M. Striccoli, A. Agostiano, R. Comparelli, N. Depalo, M. L. Curri and E. Fanizza, High Surface Area Mesoporous Silica Nanoparticles with Tunable Size in the Sub-Micrometer Regime: Insights on the Size and Porosity Control Mechanisms, *Molecules*, 2021, **26**(14), 4247.

39 A. Judefeind and M. M. De Villiers, Drug Loading into and In Vitro Release from Nanosized Drug Delivery Systems, in *Nanotechnology in Drug Delivery*, ed. M. M. De Villiers, P. Aramwit and G. S. Kwon, Springer New York, New York, NY, 2009, pp. 129–162.

40 N. Farkas and J. A. Kramar, Dynamic Light Scattering Distributions by Any Means, *J. Nanopart. Res.*, 2021, **23**(5), 120.

41 J. Lalani, D. Baradia, R. Lalani and A. Misra, Brain Targeted Intranasal Delivery of Tramadol: Comparative Study of Microemulsion and Nanoemulsion, *Pharm. Dev. Technol.*, 2015, **20**(8), 992–1001.

42 S. Tang, A. Wang, X. Yan, L. Chu, X. Yang, Y. Song, K. Sun, X. Yu, R. Liu, Z. Wu and P. Xue, Brain-Targeted Intranasal Delivery of Dopamine with Borneol and Lactoferrin Co-Modified Nanoparticles for Treating Parkinson's Disease, *Drug Delivery*, 2019, **26**(1), 700–707.

43 B. Ji, J. Maeda, M. Higuchi, K. Inoue, H. Akita, H. Harashima and T. Suhara, Pharmacokinetics and Brain Uptake of Lactoferrin in Rats, *Life Sci.*, 2006, **78**(8), 851–855.

44 A. Lopalco, A. Cutrignelli, N. Denora, A. Lopedota, M. Franco and V. Laquintana, Transferrin Functionalized Liposomes Loading Dopamine HCl: Development and Permeability Studies across an In Vitro Model of Human Blood–Brain Barrier, *Nanomaterials*, 2018, **8**(3), 178.

45 E. Ortega Martínez, M. E. Morales Hernández, J. Castillo-González, E. González-Rey and M. A. Ruiz Martínez, Dopamine-Loaded Chitosan-Coated Solid Lipid Nanoparticles as a Promise Nanocarriers to the CNS, *Neuropharmacology*, 2024, **249**, 109871.

46 R. Pahuja, K. Seth, A. Shukla, R. K. Shukla, P. Bhatnagar, L. K. S. Chauhan, P. N. Saxena, J. Arun, B. P. Chaudhari, D. K. Patel, S. P. Singh, R. Shukla, V. K. Khanna, P. Kumar, R. K. Chaturvedi and K. C. Gupta, Trans-Blood Brain Barrier Delivery of Dopamine-Loaded Nanoparticles Reverses Functional Deficits in Parkinsonian Rats, *ACS Nano*, 2015, **9**(5), 4850–4871.

47 G. G. D. L. Cruz; P. Rodríguez-Fragoso; J. Reyes-Esparza; A. Rodríguez-López; R. Gómez-Cansino and L. Rodriguez-Fragoso, Interaction of Nanoparticles with Blood Components and Associated Pathophysiological Effects, in *Unraveling the Safety Profile of Nanoscale Particles and Materials – From Biomedical to Environmental Applications*, ed. A. C. Gomes and M. P. Sarria, InTech, 2018.

48 Z.-A. Zhang, X. Xin, C. Liu, Y. Liu, H.-X. Duan, L. Qi, Y.-Y. Zhang, H. Zhao, L.-Q. Chen, M.-J. Jin, Z.-G. Gao and W. Huang, Novel Brain-Targeted Nanomicelles for Anti-Glioma Therapy Mediated by the ApoE-Enriched Protein Corona in Vivo, *J. Nanobiotechnol.*, 2021, **19**(1), 453.

49 S.-H. Jeong, J.-H. Jang and Y.-B. Lee, Drug Delivery to the Brain via the Nasal Route of Administration: Exploration of Key Targets and Major Consideration Factors, *J. Pharm. Invest.*, 2023, **53**(1), 119–152.

50 Q. Guo, H. You, X. Yang, B. Lin, Z. Zhu, Z. Lu, X. Li, Y. Zhao, L. Mao, S. Shen, H. Cheng, J. Zhang, L. Deng, J. Fan, Z. Xi, R. Li and C. M. Li, Functional Single-Walled Carbon Nanotubes 'CAR' for Targeting Dopamine Delivery into the Brain of Parkinsonian Mice, *Nanoscale*, 2017, **9**(30), 10832–10845.

51 C. V. Wrangel, K. Schwabe, N. John, J. K. Krauss and M. Alam, The Rotenone-Induced Rat Model of Parkinson's Disease: Behavioral and Electrophysiological Findings, *Behav. Brain Res.*, 2015, **279**, 52–61.

52 V. Lawana and J. R. Cannon, Rotenone Neurotoxicity: Relevance to Parkinson's Disease, in *Advances in Neurotoxicology*, Elsevier, 2020, vol. 4, pp. 209–254.

53 A. Parthasarathy, R. Hanumanthappa, S. R. Bulbule, P. C. Kiran, H. Nanjaiah, G. Gopinath, B. M. Siddaiah, D. Muniswamy and D. Kuramkote Shivanna, Stress Enhances Expression of Calcium-binding Proteins and NMDAR Subunit Genes in the Rat Hippocampus, *Neuroprotection*, 2024, **2**, 167–178.

54 Y. Hirata and T. Nagatsu, Rotenone and CCCP Inhibit Tyrosine Hydroxylation in Rat Striatal Tissue Slices, *Toxicology*, 2005, **216**(1), 9–14.

55 H. Park, T.-I. Kam, V. L. Dawson and T. M. Dawson, α-Synuclein Pathology as a Target in Neurodegenerative Diseases, *Nat. Rev. Neurol.*, 2025, **21**(1), 32–47.

56 X. Shi, H. Bai, J. Wang, J. Wang, L. Huang, M. He, X. Zheng, Z. Duan, D. Chen, J. Zhang, X. Chen and J. Wang, Behavioral Assessment of Sensory, Motor, Emotion, and Cognition in Rodent Models of Intracerebral Hemorrhage, *Front. Neurol.*, 2021, **12**, 667511.

57 D. Aksoy, V. Solmaz, T. Çavuşoğlu, A. Meral, U. Ateş and O. Erbaş, Neuroprotective Effects of Eexenatide in a Rotenone-Induced Rat Model of Parkinson's Disease, *Am. J. Med. Sci.*, 2017, **354**(3), 319–324.

58 V. Venkatesh Gobi, S. Rajasankar, M. Ramkumar, C. Dhanalakshmi, T. Manivasagam, A. Justin Thenmozhi, M. M. Essa, R. Chidambaram and A. Kalandar, *Agaricus Blazei* Extract Abrogates Rotenone-Induced Dopamine Depletion and Motor Deficits by Its Anti-Oxidative and

Anti-Inflammatory Properties in Parkinsonic Mice, *Nutr. Neurosci.*, 2018, **21**(9), 657–666.

59 A. G. Vidal-Gadea and J. T. Pierce-Shimomura, Conserved Role of Dopamine in the Modulation of Behavior, *Commun. Integr. Biol.*, 2012, **5**(5), 440–447.

60 R. Hanumanthappa, D. M. Venugopal, P. C. Nethravathi, A. Shaikh, B. M. Siddaiah, G. B. Heggannavar, A. A. Patil, H. Nanjaiah, D. Suresh, M. Y. Kariduraganavar, S. V. Raghu and K. S. Devaraju, Polyvinylpyrrolidone-Capped Copper Oxide Nanoparticles-Anchored Pramipexole Attenuates the Rotenone-Induced Phenotypes in a *Drosophila* Parkinson's Disease Model, *ACS Omega*, 2023, **8**(50), 47482–47495.

61 T. Wang, C. Li, B. Han, Z. Wang, X. Meng, L. Zhang, J. He and F. Fu, Neuroprotective Effects of Danshensu on Rotenone-Induced Parkinson's Disease Models in Vitro and in Vivo, *BMC Complementary Med. Ther.*, 2020, **20**(1), 20.

62 E. Kotsyuba and V. Dyachuk, Effects of Chronic Exposure to Low Doses of Rotenone on Dopaminergic and Cholinergic Neurons in the CNS of Hemigrapsus Sanguineus, *Int. J. Mol. Sci.*, 2024, **25**(13), 7159.

63 R. K. Singh, K. D. Patel, C. Mahapatra, S. P. Parthiban, T.-H. Kim and H.-W. Kim, Combinatory Cancer Therapeutics with Nanoceria-Capped Mesoporous Silica Nanocarriers through pH-Triggered Drug Release and Redox Activity, *ACS Appl. Mater. Interfaces*, 2019, **11**(1), 288–299.

64 Y. Wei, L. Gao, L. Wang, L. Shi, E. Wei, B. Zhou, L. Zhou and B. Ge, Polydopamine and Peptide Decorated Doxorubicin-Loaded Mesoporous Silica Nanoparticles as a Targeted Drug Delivery System for Bladder Cancer Therapy, *Drug Delivery*, 2017, **24**(1), 681–691.

65 A. Lopalco, A. Cutrignelli, N. Denora, A. Lopedota, M. Franco and V. Laquintana, Transferrin Functionalized Liposomes Loading Dopamine HCl: Development and Permeability Studies across an In Vitro Model of Human Blood–Brain Barrier, *Nanomaterials*, 2018, **8**(3), 178.

66 G. B. Heggannavar, C. G. Hiremath, D. D. Achari, V. G. Pangarkar and M. Y. Kariduraganavar, Development of Doxorubicin-Loaded Magnetic Silica–Pluronic F-127 Nanocarriers Conjugated with Transferrin for Treating Glioblastoma across the Blood–Brain Barrier Using an in Vitro Model, *ACS Omega*, 2018, **3**(7), 8017–8026.

67 Q. Bao, P. Hu, Y. Xu, T. Cheng, C. Wei, L. Pan and J. Shi, Simultaneous Blood–Brain Barrier Crossing and Protection for Stroke Treatment Based on Edaravone-Loaded Ceria Nanoparticles, *ACS Nano*, 2018, **12**(7), 6794–6805.

68 Z. Wang, C. Zhang, F. Huang, X. Liu, Z. Wang and B. Yan, Breakthrough of ZrO_2 Nanoparticles into Fetal Brains Depends on Developmental Stage of Maternal Placental Barrier and Fetal Blood-Brain-Barrier, *J. Hazard. Mater.*, 2021, **402**, 123563.

69 M. R. Smruthi, I. Nallamuthu and T. Anand, A Comparative Study of Optimized Naringenin Nanoformulations Using Nano-Carriers (PLA/PVA and Zein/Pectin) for Improvement of Bioavailability, *Food Chem.*, 2022, **369**, 130950.

70 A. Magdy, E. A. E. Farrag, S. M. Hamed, Z. Abdallah, E. M. El Nashar, M. A. Alghamdi, A. A. H. Ali and M. Abd El-kader, Neuroprotective and Therapeutic Effects of Calcitriol in Rotenone-Induced Parkinson's Disease Rat Model, *Front. Cell. Neurosci.*, 2022, **16**, 967813.

71 S. L. Neha, A. K. Mishra, L. Rani, S. Paroha, H. K. Dewangan and P. K. Sahoo, Design and Evaluations of a Nanostructured Lipid Carrier Loaded with Dopamine Hydrochloride for Intranasal Bypass Drug Delivery in Parkinson's Disease, *J. Microencapsulation*, 2023, **40**(8), 599–612.

72 S. Ojha, H. Javed, S. Azimullah, S. B. Abul Khair and M. E. Haque, Glycyrrhizic Acid Attenuates Neuroinflammation and Oxidative Stress in Rotenone Model of Parkinson's Disease, *Neurotoxic. Res.*, 2016, **29**(2), 275–287.

73 T. Fujikawa, N. Kanada, A. Shimada, M. Ogata, I. Suzuki, I. Hayashi and K. Nakashima, Effect of Sesamin in Acanthopanax Senticosus HARMS on Behavioral Dysfunction in Rotenone-Induced Parkinsonian Rats, *Biol. Pharm. Bull.*, 2005, **28**(1), 169–172.

74 S. Kumar, S. Kumar, R. Arthur and P. Kumar, Trans-Cinnamaldehyde Mitigates Rotenone-Induced Neurotoxicity via Inhibiting Oxidative Stress in Rats, *Pharmacol. Res. – Mod. Chin. Med.*, 2023, **6**, 100209.

75 H.-C. Tseng, M.-H. Wang, C.-H. Fang, Y.-W. Lin and H.-S. Soung, Neuroprotective Potentials of Berberine in Rotenone-Induced Parkinson's Disease-like Motor Symptoms in Rats, *Brain Sci.*, 2024, **14**(6), 596.

76 R. Hanumanthappa, D. M. Venugopal, P. C. Nethravathi, A. Shaikh, B. M. Siddaiah, G. B. Heggannavar, A. A. Patil, H. Nanjaiah, D. Suresh, M. Y. Kariduraganavar, S. V. Raghu and K. S. Devaraju, Polyvinylpyrrolidone-Capped Copper Oxide Nanoparticles-Anchored Pramipexole Attenuates the Rotenone-Induced Phenotypes in a *Drosophila* Parkinson's Disease Model, *ACS Omega*, 2023, **8**(50), 47482–47495.